# Fault friction during simulated seismic slip pulses

**Christopher Harbord[1], Nicolas Brantut[1], Elena Spagnuolo[2] and Giulio Di Toro[3]**

[1]Department of Earth Sciences, University College London, London, UK,

[2] Istituto Nazionale di Geofisica e Vulcanologia, Via di Vigna Murata 605, Rome, Italy,

[3] Dipartimento di Geoscienze, Università degli studi di Padova, Padua, Italy

Corresponding author: Christopher Harbord (c.harbord@ucl.ac.uk)

**Key Points:**

- We investigate the evolution of fault strength during realistic earthquake slip history
- The high velocity strength of carbonate built faults is compatible with flash heating at short timescales and viscous creep rheology at larger timescales.
- We document limited elastodynamic compatibility between measured fault strength and imposed slip history

## Abstract

Theoretical studies predict that during earthquake rupture faults slide at non-constant slip velocity, however it is not clear which source time functions are compatible with the high velocity rheology of earthquake faults. Here we present results from high velocity friction experiments with non-constant velocity history, employing a well-known seismic source solution compatible with earthquake source kinematics. The evolution of friction in experiments shows a strong dependence on the applied slip history, and parameters relevant to the energetics of faulting scale with the impulsiveness of the applied slip function. When comparing constitutive models of strength against our experimental results we demonstrate that the evolution of fault strength is directly controlled by the temperature evolution on and off the fault. Flash heating accurately predicts weakening behaviour at short timescales, but at larger timescales strength is better predicted by a viscous creep rheology. We use a steady-state slip pulse to test the compatibility of our strength measurements at imposed slip rate history with the stress predicted from elastodynamic equilibrium. Whilst some compatibility is observed, the strength evolution indicates that slip acceleration and deceleration might be more rapid than that imposed in our experiments.


## 1 Introduction

During earthquakes, faults weaken abruptly, and slip accelerates to velocities of the order of several metres per second (Kanamori & Brodsky, 2004; Madariaga, 2015). The exact stress and slip evolution on faults is rarely well constrained by seismological observations, which can generally only provide estimates of integrated quantities, such as average stress drop and slip,

breakdown work and radiated energy (Abercrombie & Rice, 2005; Guatteri & Spudich, 2000; Kanamori & Rivera, 2006).

Fault slip can be quite complex during earthquakes, with highly variable velocity history. Models and experimental observations based on fracture mechanics exhibit the common feature of a a rapid acceleration to a peak velocity, corresponding to the passage of the rupture tip, after which slip rate decays to zero (see theoretical overview in Scholz, 2002, Section 4.2; early laboratory work by Okubo & Dieterich, 1981; Ohnaka et al., 1986, and more recent work by Rubino et al., 2017; Berman et al., 2020, among many others). Kinematic source models inverted from seismological data are often nonunique and require significant smoothing due to the relatively low frequency data used; specific choices have to be made for the general functional form of the slip history for fault patches, but the corresponding dynamic stress evolution (and associated derived quantities, e.g., fracture energy) strongly depends on such model choices (Guatteri & Spudich, 2000; Tinti et al., 2005). It remains unclear what source-time function would best correspond to the actual traction evolution along the fault. Tinti et al. (2005) used theoretical considerations to develop a source-time function that is compatible with elastodynamics, but it is not guaranteed that such theoretical slip function leads to traction evolution that is compatible with the rheology of the fault. Attempts have been made to verify this compatibility by comparing high velocity fault rheology obtained in laboratory experiments with earthquake source parameters estimated from strong motion seismograms, with limited success (Chang et al., 2012; Fukuyama & Mizoguchi, 2010).

In nature, there is a feedback between the slip rate on the fault (associated with a given stress state through elastodynamic equilibrium) and the shear strength of the fault zone materials. A substantial body of work has shown that fault strength is dramatically lower at rapid deformation rates in comparison to that during slow interseismic deformation (Faulkner et al., 2011; Goldsby & Tullis, 2011; Han et al., 2007; Brantut et al., 2008; Hirose & Shimamoto, 2005; Di Toro et al., 2011). The low strength observed during rapid deformation in the laboratory can explain the propagation of ruptures in numerical models (Noda et al., 2009; Noda & Lapusta, 2013), and is quantitatively consistent with the low heat flow and shear heating estimated from borehole measurements after the 2011 Tohoku-oki earthquake (Fulton et al., 2013; Ujie et al., 2013). High velocity friction experiments have shown that sliding velocity exerts a first order control in governing the strength of faults (Goldsby & Tullis, 2011; Han et al., 2007; Di Toro et al., 2004, 2011; Tsutsumi & Shimamoto, 1997). Several physical models have been proposed to explain this weakening. Nielsen et al. (2008, 2010) developed a model of frictional melting in basic igneous rocks which showed good agreement with the experimental data of Hirose & Shimamoto (2005). The flash heating model (FH), based on frictional heating at microscale contacting asperities (Rice, 2006; Beeler et al., 2008), was successful in explaining experimental observations in crystalline felsic rocks in the absence of bulk frictional melting (Goldsby and Tullis, 2011) . More recently in carbonate rocks, grain size sensitive creep has been proposed to explain the weakening behaviour due to the presence of nanometric grains which facilitate rapid diffusive mass transfer (Demurtas et al., 2019; De Paola et al., 2015; Pozzi et al., 2018).

Although velocity exerts a direct control on fault strength, a number of studies have also demonstrated the important role of fault slip history in determining strength evolution: In particular, hysteresis in the frictional strength has been systematically observed between

acceleration and deceleration phases of experiments, suggesting a change in the physical state of the fault during experiments (e.g., Goldsby & Tullis, 2011; Proctor et al., 2014; Sone & Shimamoto, 2009). A number of authors have shown that this difference can be accounted for by considering the temperature rise of the fault as a state variable in FH models (Proctor et al., 2014). By controlling the thermal evolution of gouge material during high velocity friction tests Yao et al. (2016) demonstrated the key role of temperature in high velocity weakening mechanisms. In parallel, experimental data and modelling by Passelègue et al. (2014) showed that subtle effects of temperature variations on fault rock properties, such as thermal conductivity, could lead to significant effects on fault weakening.

Given that temperature evolution is directly coupled to slip history and strength through dissipation of mechanical energy, the strength evolution and the resulting dynamics of earthquakes are expected to be controlled by thermo-mechanical feedbacks.

Here, we aim to investigate the role of slip history on the the frictional response of rocks, and test the compatibility of laboratory-derived strength evolution with elastodynamics. We use a slip history that is representative of earthquake source-time functions in the form of a so-called "modified Yoffe function" as derived by Tinti et al. (2005) (see Methods section), and test a range of initial accelerations for a fixed total slip (Figure 1). We first explore the physical mechanisms that give rise to the observed complex frictional response, and show that thermally-activated mechanisms like flash heating (near the onset of the slip) and viscous creep (at late stages) are broadly consistent with the observed frictional response. This agreement confirms the key role of temperature and temperature history in the high velocity frictional behaviour of rocks. We then analyse the compatibility of our experimental results with the traction evolution

expected from a simple elastodynamic slip pulse model. The measured frictional response is not totally consistent with the model in that it shows more abrupt weakening at the onset of slip and too large re-strengthening at the termination of slip. These differences indicate that elastodynamics would likely produce either shorter slip pulses or sharper drops in slip rate at the tail end of pulses (self-healing).

## 2 Methodology

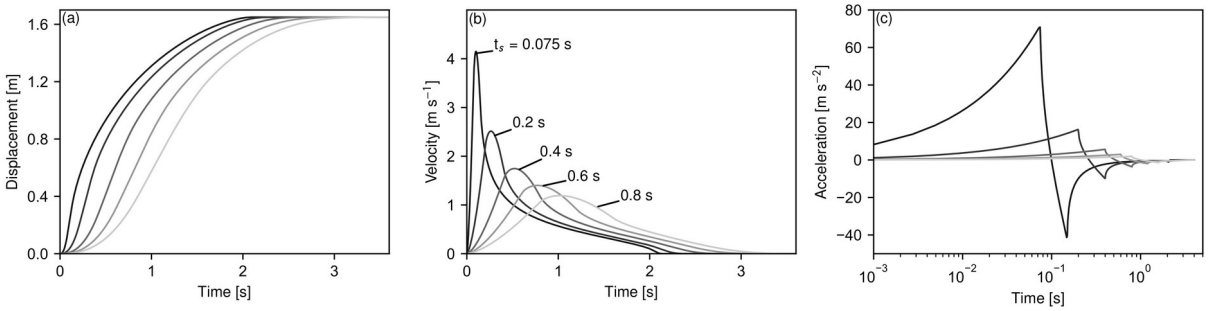


**Figure 1** Yoffe function slip plotted as a function of time (a) and associated temporal derivatives, velocity (b) and acceleration (c) imposed during experiments presented in this manuscript, functions were produced following the closed form solution in Tinti et al. (2005). Here $t_s$ is the smoothing time (see main text).

Our experiments are analogous to slip on a single point on a fault, and we therefore need to select an appropriate slip function representative of a rupture propagating through a single point in space. In practise it is not possible to define a unique solution since fault slip history depends on the interactions between fault strength and elastodynamics, however there are several candidates we may choose to represent the seismic source (Kostrov, 1964; Madariaga & Nielsen, 2003;Tinti et al., 2005; Yoffe, 1951). The Yoffe function represents an attractive solution to model slip history due to its direct compatibility with elastodynamic rupture propagation (Nielsen & Madariaga, 2003; Tinti et al., 2005), and the fact that it shares similarity to slip histories observed in experimental studies (Berman et al., 2020; Rubino et al., 2017). It is characterised by a singular acceleration at the moving crack tip, corresponding to the crack tip

126 stress concentration, followed by an inverse square-root decay in velocity with respect to time
127 (Figure 1b). This results in slip that is approximately square root in time at a fixed observation
128 locality (Figure 1a). Given that singular acceleration is unrealistic in nature, and also not possible
129 to simulate in the laboratory, we used a regularised form of the Yoffe function presented in Tinti
130 et al. (2005). The solution is equivalent to convolving a true Yoffe function (with singular
131 acceleration) with a triangular function of time duration, $t_s$, defined as the smoothing time. Small
132 values of the smoothing time generate more impulsive, shorter duration events i.e. faster initial
133 accelerations, and increasing $t_s$ generates longer duration, less impulsive events (Figure 1). In
134 experiments, the rise time $t_r$= 2 s, and maximum displacement, $U_{tot}$ = 1.65 m, were kept constant,
135 to simulate seismic slip equivalent to a typical $M_w$ = 7 earthquake (Wells and Coppersmith,
136 1994). We varied $t_s$ from 0.05 to 0.8 s, which may be considered analogous to varying the
137 rupture velocity (Cochard & Madariaga, 1994).
138
139 We utilised a slow to high velocity rotary shear apparatus (SHIVA, Di Toro et al., 2010)
140 installed in the HPHT laboratory at INGV in Rome. The apparatus is capable of applying up to
141 70 kN of axial load using an electromechanical piston (Bosch-Rexroth EMC105HD), which is
142 servo controlled at a frequency of 8 kHz. A 300 kW motor servo-controlled at 16 kHz drives the
143 rotary motion up to 3000 RPM, we achieved an instantaneous acceleration of <80 m/s$^2$ and a
144 deceleration of <60 m/s$^2$ (figure 1c); outside of this range machine vibrations were too strong to
145 gather reliable data. Displacement was measured using a high resolution encoder (6297600 divs)
146 for low velocity (< 0.15 m/s) and a low resolution encoder (4000 divs) for high velocity (≥0.15
147 m/s), the encoder-derived velocity (Figure 2 grey curves) and the imposed velocity function
148 (Figure 2 black curves) show good agreement. Annular cohesive samples of Etna basalt and

149 Carrara marble of 50 mm external and 30 mm internal diameter were prepared for testing, and
150 were squared using a lathe before being ground with #80 grit prior to experimentation. All tests
151 were performed at a normal stress of 10 MPa. Torque was measured using an S-type load cell on
152 the stationary side of the apparatus and all data was logged at 12.5 kHz. A total of over 60
153 simulated slip events are presented in this study (see section 1 in supplementary material). In the
154 majority of experiments slip pulses were repeated using the same sample, with the normal load
155 kept constant during a minimum time period of at least 20 minutes between individual pulses.
156

## 3 Experimental results

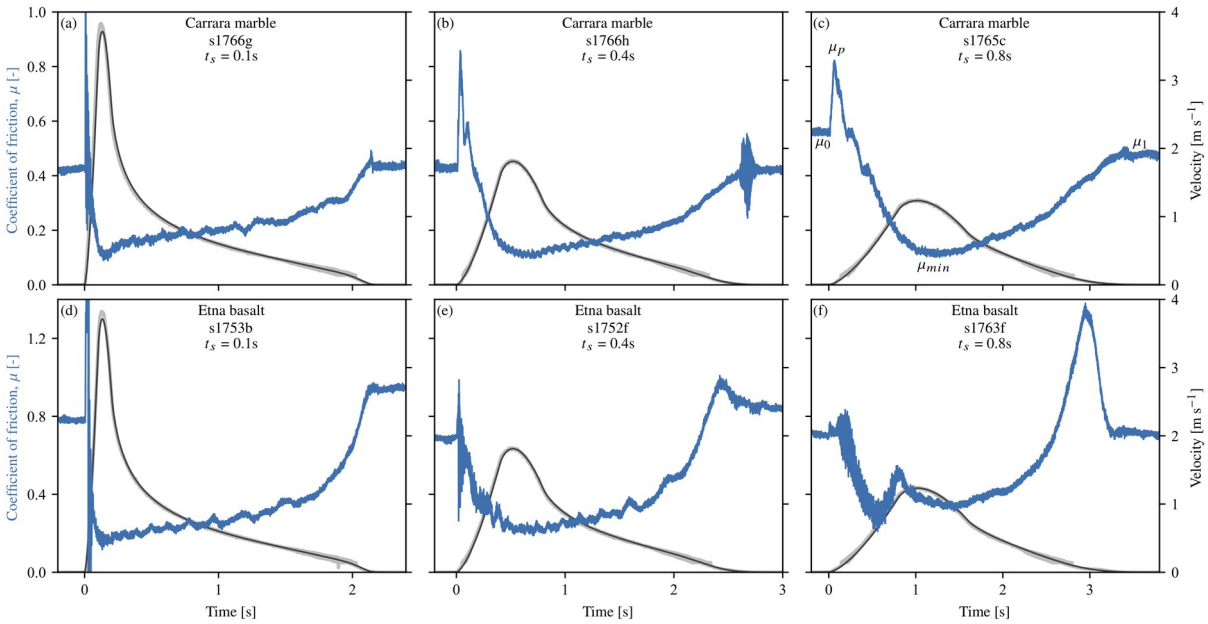


**Figure 2** Frictional response of simulated faults during application of Yoffe functions of varying smoothing time. Panels a)-c) show Carrara marble with increasing values of the smoothing time from left to right (0.1 to 0.8), panels d)-f) show Etna basalt frictional response for the same slip histories as a)-c). Velocity history is shown for reference, where the thicker grey curve represents the encoder derived velocity history, and the black the imposed control signal. Panel c) is labelled according to the frictional parameters identified in the main text.

All experiments show three stages of behaviour typical of high velocity friction tests: (i) An elastic loading and slip-strengthening phase, which corresponds to an increase in friction coefficient from an initial value at zero velocity, $\mu_0$ = 0.5–0.6 ($\tau_0$ = 5–6 MPa), to a peak as slip rate increases, $\mu_p$ = 0.6–0.8 ($\tau_p$ = 6–8 MPa, Figures 2b and 2c); (ii) A breakdown phase past the peak in frictional strength, where friction drops from $\mu_p$ to a minimum weakened value, $\mu_{min}$, which is generally coeval with the peak in velocity. Values of $\mu_{min}$ are typical of high velocity friction, with values around $\mu_{min}$ = 0.05–0.2 ($\tau_{min}$ = ¿0.5–2 MPa) in marble (Figure. 2a)-c)), and $\mu_{min}$ = 0.2–0.3 ($\tau_{min}$ = 2–3 MPa) in Etna basalt (Figure 2d)-e)); (iii) A final slip restrengthening

176 phase, where frictional strength increases steadily to a final value, $\mu_1$, as slip rate decelerates,
177 corresponding to the end of the experiment. In Carrara marble the strength typically recovers to
178 $\mu_1$ = 0.4–0.5 ($\tau_1$= 4–5 MPa, Figure 1a-c), by contrast, for Etna Basalt the strength recovery can
179 become large during deceleration, increasing with $t_s$ (Figure 2d and f). At the largest values of $t_s$
180 = 0.8s, during the restrengthening phase, the frictional strength in basalt reaches an apparent
181 value of μ = 1–1.2 (10–12 MPa), before reducing to μ = 0.6–0.9 (6–9 MPa). In tests where this
182 behaviour was observed the sample often failed in a brittle manner with audible cracking coeval
183 with the peak in friction.
184
185 When comparing between experiments we observe a clear dependence between the overall
186 frictional behaviour and the imposed smoothing time. Inspection of tests with $t_s$ = 0.1s (A ≈60m/
187 $s^2$, Figure 2a) and d)) shows an almost instantaneous drop in friction, with weakening achieved
188 on a timescale similar to $t_s$. As $t_s$ is increased from 0.1 to 0.4s (Figure 2b) and e)) we observe an
189 increase in the weakening timescale, and by extension an increase in the weakening distance.
190 This trend continues to the largest values of $t_s$ = 0.8 (A ≈0.7m/$s^2$ Figure 2c) and f)), where the
191 weakening timescale is of similar value to $t_s$. In order to quantify how the smoothing time $t_s$
192 influences the overall mechanical behaviour of the simulated faults, we now estimate key
193 quantities relevant to the energetics of faulting.

194 3.1 Weakening distance

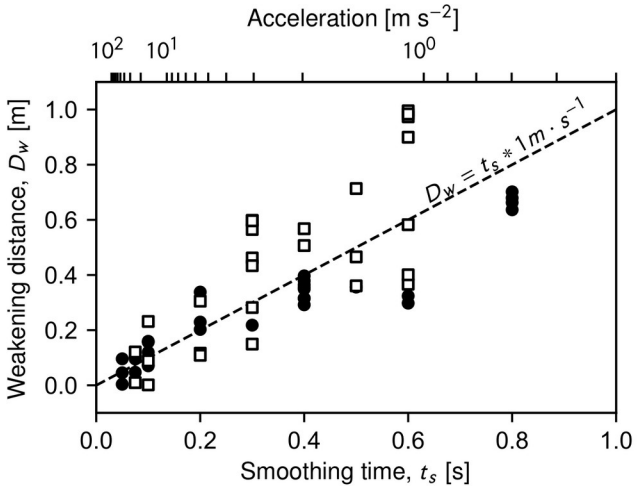


195

196 **Figure 3** Scaling of the weakening distance with the smoothing time, $t_s$. Filled circles represent
197 measurements derived from experiments with Carrara marble, open square symbols are Etna
198 Basalt. The top scale shows the acceleration rate, $A = V_{max}/t_s$, corresponding to the smoothing
199 timescale on the bottom x-axis defined by the relationship $A = 0.5t_s^{-1.5}$.

200 The coseismic weakening distance is an important parameter governing the propagation of
201 earthquake rupture, providing an indication of rupture efficiency (Ida, 1972). It may also provide
202 insight into the weakening mechanisms active during experiments (Hirose & Shimamoto, 2005;
203 Niemeijer et al., 2011). To estimate the weakening distance, $D_w$, we consider the distance at
204 which strength decreases by 95% and use the same formulation as Hirose & Shimamoto (2005)
205 and fit data using a least squares regression. The fitted values range from 0.05–1 m for the
206 presented experiments (see supplementary table S1), and are strongly dependent on the slip
207 function applied, but are within the range of values presented in previous studies under similar
208 experimental conditions (Chang et al., 2012; Niemeijer et al., 2011). A clear trend is observed
209 between $t_s$ and $D_w$ (Figure 3), given that smaller values of $t_s$ correspond to a larger acceleration
210 demonstrating an inverse dependence on the initial acceleration. For example, for Carrara marble
211 (Figure 3 filled circles), at $t_s$ =0.05s ($A \approx 80 m/s^2$) $D_w$ = 0.08 m, whereas for $t_s$= 0.8 ($A \approx 0.7 m/s^2$),
212 the weakening distance increases to $D_w$ =0.6 m, representing an order of magnitude change. A

similar order of magnitude increase is observed in Etna basalt (Figure 3, open squares), with $D_w$ = 0.1m at $t_s$ =0.1s (A ≈16 m/s$^2$), increasing to $D_w$ = 0.5-0.9m at $t_s$ =0.8s (A ≈0.7m/s$^2$). It should be noted that values of $D_w$ for Etna basalt become increasingly scattered as $t_s$ increases.

### 3.2 Energy dissipation

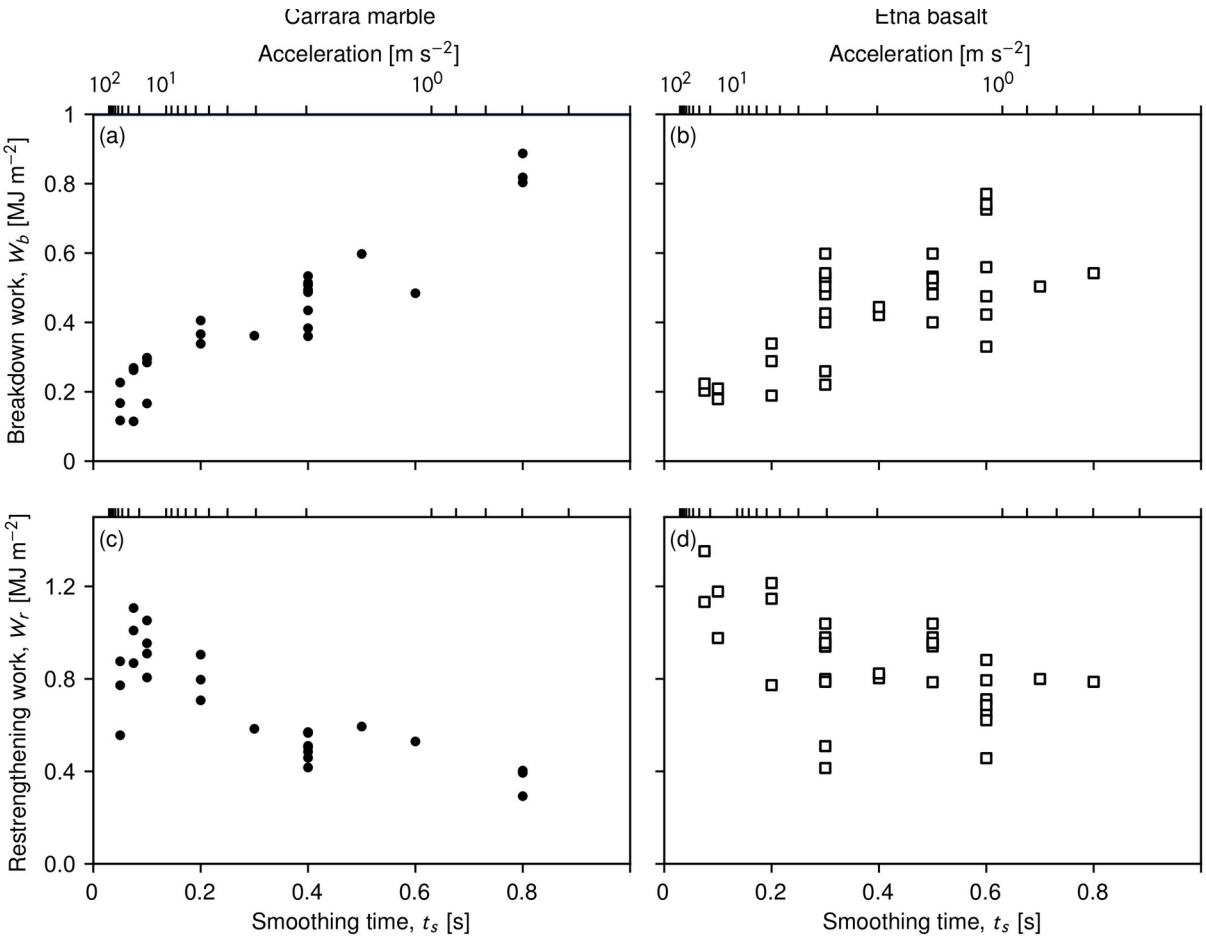


**Figure 4** Partitioning of breakdown work (a) and c)) and restrengthening work (b) and d)) during simulated Yoffe pulses of varying initial acceleration rates for Carrara marble (a) and b)) and Etna Basalt (c) and d)).

Following previous literature, we define the breakdown work $W_b$ [MJ m$^{-2}$], according to the general definition of Abercrombie & Rice (2005),

$$W_b = \int_0^{D_w} \left[ \tau(D) - \tau_{min} \right] dD, \quad (1)$$

Where $D_w$ is the displacement when $\tau = \tau_{\min}$. We also define restrengthening work, $W_r$, in a similar manner, accordingly:

$$W_r = \int_{D_w}^{D_{tot}} \left[ \tau(D) - \tau_{min} \right] dD, \quad (2)$$

Both of these parameters were calculated by numerical integration of the experimental shear stress record with respect to slip (see Nielsen et al., 2016). This provides a quantitative estimate of energy partitioning during experiments. We find that both $W_b$ and $W_r$ depend strongly on the impulsiveness of the Yoffe function applied. Faster initial acceleration rates result in smaller values of $W_b$ and larger $W_r$ (Figure 4). For example for $t_s$ = 0.075s ($A \approx 80$m/s$^2$), $W_b$ = 0.2 MJ/m$^2$ for both marble (Figure 4a) and basalt (Figure 4c), whereas for $t_s$ =0.8s ($A \approx 1$m/s$^2$), $W_b$ = 0.8 MJ/m$^2$ for marble and $W_b$ = 0.9 MJ/m$^2$ for basalt. An inverse relationship is observed for the restrengthening, with shorter deceleration time periods generally resulting in a reduction in $W_r$ (Figure 4b and c). For example when $t_s$ = 0.8, $W_r$ = 0.3 and 0.4 MJ/m$^2$ for marble and basalt respectively, and for $t_s$ = 0.1, $W_r$ increases to 1.2 and 1.4 MJ/m$^2$ for marble and basalt respectively. The restrengthening work is generally larger for basalt than it is for marble for a given $t_s$ or initial acceleration rate.

## 4 Driving processes of frictional evolution in the presence of complex slip velocity histories

Our results show that strong variations in slip rate induce correspondingly strong variations in frictional strength, with a rapid weakening at high slip rate and significant restrengthening as slip rate decreases. In order to identify the key driving mechanisms responsible for these variations, here we test whether such variations are captured and predicted by existing physics-based high velocity friction laws.

One key experimental observation is that the minimum strength is almost systematically occurring at the peak velocity achieved during the tests (Figure 2), which corresponds to a velocity-weakening behaviour of the rocks. Such a behaviour is typically associated with some state evolution, whereby instantaneous changes in slip rate should induce strength increase, followed by adjustments towards a lower strength state. Here, the observation of direct correlation between peak slip rate and minimum strength indicates that this state evolution occurs over time (and slip) scales much smaller than that of the change in slip rate imposed in the experiments. This is consistent with models where state was assumed to evolve over slip distances of the order of tens of microns, indeed much shorter than the slip scales measured here (e.g. Noda et al., 2009). Therefore, we primarily focus on a description of strength that excludes considerations of short-slip state evolution.

Firstly, we focus on predicting the strength of experiments using Carrara marble. We explore two commonly proposed descriptions of strength, flash heating (Goldsby & Tullis, 2011; Proctor et al., 2014; Yao et al., 2016) and grain size sensitive creep (De Paola et al., 2015; Pozzi et al.,

2018; Violay et al., 2019), focussing on accurately modelling experimental boundary conditions. Then we discuss the frictional behaviour of Etna basalt hosted faults, and provide a simple comparison to previous models of high velocity friction for melt accommodated weakening.

## 4.1 Flash heating

Weakening by flash heating (FH) is based on the idea that contacting asperities at the sliding interface dramatically weaken at some threshold temperature (Beeler et al., 2008; Rice, 2006). High velocity experimental data obtained using simple slip rate histories have been shown to be in general agreement with this model (Goldsby & Tullis, 2011; Proctor et al., 2014; Yao et al., 2016). The shear strength is assumed to be given by $\tau = f\,\sigma_n$, where the friction coefficient $f$ behaves as

$$f = f_w + (f_0 - f_w)\frac{V}{V_w(T - T_w)}, \quad (3)$$

$f_0$ is the low velocity coefficient of friction, $f_w$ the weakened coefficient of friction and $V_w$ a critical weakening velocity that depends on the difference between the ambient fault temperature $T$ and a critical weakening temperature $T_w$. The critical velocity defines a threshold at which a contacting asperity spends a portion of its lifetime above the prescribed temperature $T_w$ corresponding to some weakening process, e.g., mineral decomposition (see Supplementary material section 2 for further details). Here we also explore the impact of temperature dependent asperity strength and size, which vary according to an asperity stress exponent, $n$.

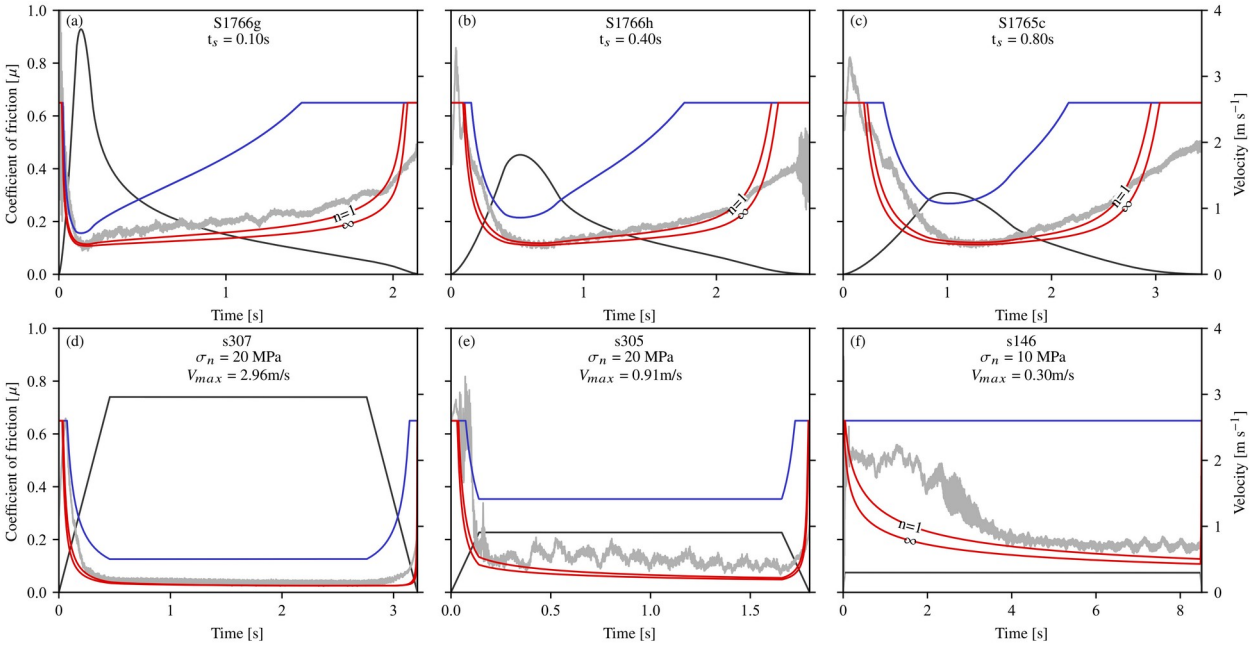


**Figure 5** Flash heating models compared to experiments with Carrara marble. Blue curves represent a purely velocity dependant friction law, red curves indicate models where background temperature rise considered. Curves are labelled according to the value of the asperity stress exponent. Insets a) to c) represent experiments conducted with Yoffe slip histories, whereas d) to f) are reproduced from *Violay et al. (2013)* and were conducted with box-car slip histories.

Using the velocity histories imposed in the experiments, we first modelled fault strength with a fixed ambient temperature (Figure 5, blue curves), i.e., purely velocity-dependent strength. Comparison of this model directly with our experimental data shows that for all cases, purely velocity dependant strength is initially consistent with weakening behaviour but diverges with increasing time. When fully accounting for the rise in background temperature, modelled by introducing the bulk heat dissipation and diffusion in the rock (e.g., Proctor et al., 2014; see Supplementary Materials, Section 2), the model predictions significantly improve (Figure 5 red curves), and strength predictions are generally accurate at short timescales ($t < 2s$). However, the models still tend to diverge from the data at larger timescales. Particularly good model agreement is found for the shortest duration Yoffe slip history experiment (Figure 5a), with the strength well predicted by the numerical models. The flash heating model does not match

297 restrengthening well for any of the experiments conducted with yoffe velocity history. Changes
298 in the value of the asperity stress exponent result in marginal changes to the strength predictions,
299 when n = 1 the predicted weakening is slower, and strength recovery onsets earlier, reflecting the
300 dominance of asperity strength loss in similarity to Passelègue et al. (2014).
301
302 To place the modelling results in the context of previous results we also compiled data from
303 experiments performed at similar conditions in SHIVA, where 'box-car' slip histories i.e.
304 constant acceleration to constant velocity followed by a constant deceleration to zero velocity,
305 were employed (Violay et al., 2013, 2019). Experiments run at a range of velocities are
306 reproduced and compared to models of flash heating (Figure 5d-f), and are shown to highlight
307 that all model predictions tend to overlap at high constant velocity. This overlap tends to
308 obfuscate the determination of realistic model parameters, particularly at the highest velocities, at
309 least for the range considered here. At relatively low velocity conditions differences are observed
310 between individual models (V = 0.3 m/s, Figure 5f). In agreement with experiments where slip
311 rate was given by Yoffe functions, we observe that a reasonable prediction of data can be
312 obtained when n = 1.
313
314 A consistent observation in all flash heating models is that they significantly over-predict the
315 restrengthening behaviour, and demonstrate that addition of temperature dependant asperity
316 properties does not significantly improve the prediction of strength. An improvement may be
317 yielded by accounting for a log normal distribution of asperity sizes which is a smooth function
318 of velocity (Beeler et al., 2008), which may be more representative of the geometry of
319 experimental surfaces (Candela & Brodsky, 2016).
320

## 4.2 Grain size sensitive creep

Another proposed model of high velocity fault strength in Calcite rich faults is grain size sensitive creep (GSS). This is motivated by observations of nanometric grains within experimental and natural fault zones coupled to the expectation of high temperatures resulting from frictional heating of the slip zone (Demurtas et al., 2019; De Paola et al., 2015; Pozzi et al., 2018). Here we check consistency of our data with direction predictions from a GSS creep law derived from deformation of fine grain calcite aggregates at high pressure temperature conditions (Schmid et al., 1977):

$$\tau \propto \dot{\gamma} d^{-m} e^{\frac{E_a}{RT}}, \quad (4)$$

where $\dot{\gamma}$ is the shear strain rate, $d$ is the grain size, $m$ is the grain size exponent, $E_a$ is the activation energy and $R$ is the gas constant (see Supplementary material S1, for detailed parameter values and modelling assumptions). Similarly to our computations using flash heating, we fully account for the background temperature evolution in the rock with temperature

dependant thermal diffusivity.

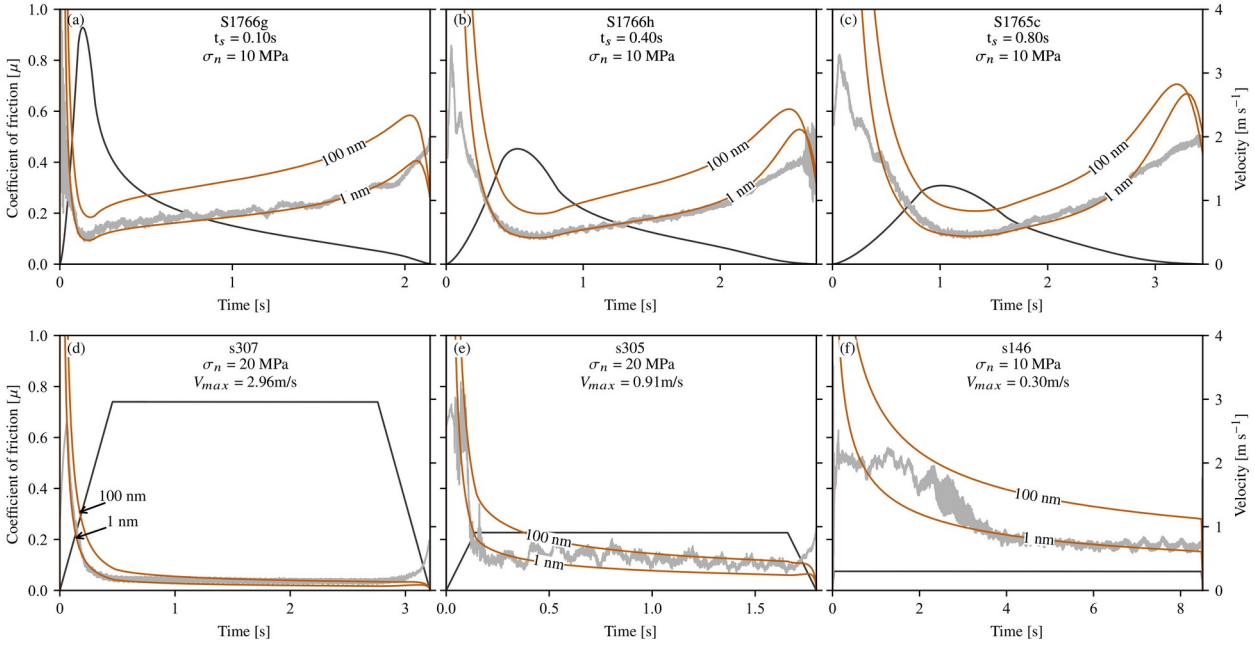


**Figure 6** GSS creep models (red) compared with experimental data (grey solid lines). Curves are labelled according to grain size used in model runs. Insets a) to c) are Yoffe slip history experiments and d) to f) are reproduced experiments from *Violay et al. (2013)* with "box-car" slip histories. All experiments are the same as in figure 5.

340 Results from GSS models systematically overpredict the strength of faults at short timescales,
341 and do not predict the initial weakening for all values of $t_s$ (Figure 6a, b and c). However, from
342 the late stages of weakening, up to the later stages of restrengthening we observe a good
343 prediction of strength evolution. When $t_s$ = 0.1 s the restrengthening is well matched, however
344 for larger values of $t_s$ = 0.4 s and 0.8 s, GSS models systematically predict a faster
345 restrengthening rate during the final deceleration period than experiments. At cessation of slip, as
346 velocity decreases below ~1 mm/s, the model predicts a complete loss of strength at all
347 conditions consistently with the GSS flow law (Figure 6a, b and c). The prediction of zero
348 strength when compared to the experimental data suggests that GSS may no longer
349 accommodate deformation during the final stages of slip. A grain size of 1 nm is systematically
350 required to predict the strength of faults with Yoffe velocity history (Figure 6 a-c). Again, for
351 comparison purposes, results are shown from Violay et al., (2013) and Violay et al., (2019). With
352 GSS models a reduced degree of convergence is observed at constant velocity, although the same
353 grain sizes show a generally similar behaviour at large timescales where sliding velocity is high
354 (V >= 1 m/s, Figure 6d and e). A reasonable agreement between models and data is observed for
355 a box-car slip history at velocity of 0.3 m/s (fig 6f), identifying the wider applicability of the
356 creep model across the range of sliding velocities. Again, 1 nm grain sizes are required to
357 accurately predict the strength of experiments conducted with a box car velocity history at low
358 velocity, low normal stress conditions (Figure 6f), however use of a 100 nm grain size shows
359 good agreement with the higher velocity experiments (fig 6d and e).
360
361 The nanometric grain size required to match fault strength is probably unrealistic (De Paola et
362 al., 2015; Pozzi et al., 2018; Violay et al., 2013). However, this could be remedied by using a

363 modified, much larger value for the preexponential factor in Equation 4; here, we decided to use
364 an empirical estimate from an exisiting dataset obtained at low strain rate, but several physical
365 phenomena might dramatically change that value. Pre-exponential factors include contributions
366 from grain boundary geometry (thickness and roughness) and grain boundary self-diffusion
367 (Poirier, 1985). It is possible that the fault microstructure during initial weakening, which has
368 been demonstrated to result from dislocation avalanches (Spagnuolo et al., 2015), may result in
369 anhedral nanograins with larger grain boundary aspect ratio when compared to the final
370 microstructure which is likely to have annealed during cooling of the fault. Raj & Ashby (1971)
371 demonstrated that increases in the aspect ratio of contacting grain boundaries increases the self-
372 diffusion coefficient, resulting in reduced yield stress, which may preclude the need for
373 unrealistically small grain sizes.
374
375 It is also important to consider that if flash processes occur during initial fault weakening,
376 temperature may be locally higher than predicted from GSS models. An initial flux of heat
377 resulting from asperity-scale processes may be sustained throughout the test duration (Aretusini
378 et al., 2020), which would allow larger grain sizes to give quantitative agreement with the
379 experimental data. We also note that in Violay et al. (2019) the authors were able to match the
380 final fault restrengthening of the data presented in Figure 6d) by accounting for heat loss in two
381 dimensions.
382

## 383 4.3 The importance of accurate temperature history

384
385 Both the flash heating and grain size sensitive creep models demonstrate the importance of
386 incorporating temperature history into the models, and shows that it is important to consider

appropriate thermal properties in model boundary conditions. This point was first highlighted by Yao et al. (2016) where experiments were conducted using sample holders of varying thermal diffusivity, demonstrating that varying temperature histories give differing strength evolutions. Here we further test this hypothesis by comparing the output of both FH and GSS models by using previously published calcite gouge experimental data obtained with a range of sample holders of varying diffusivity (Cverna, 2002). We consider, in order of increasing thermal diffusivity, grade 4 Titanium alloy (Ti90Al6V4, Pozzi et al., 2018), AISI 316 stainless steel (De Paola et al., 2015) and tungsten carbide (Smith et al., 2013). We approximate each experimental geometry as closely as possible in 1D, with the principal slip zone localised asymmetrically on the boundary between the gouge layer and the sample holder with appropriate thermal diffusivity (De Paola et al., 2015; Pozzi et al., 2018a; Smith et al., 2013, see supplementary material S1).

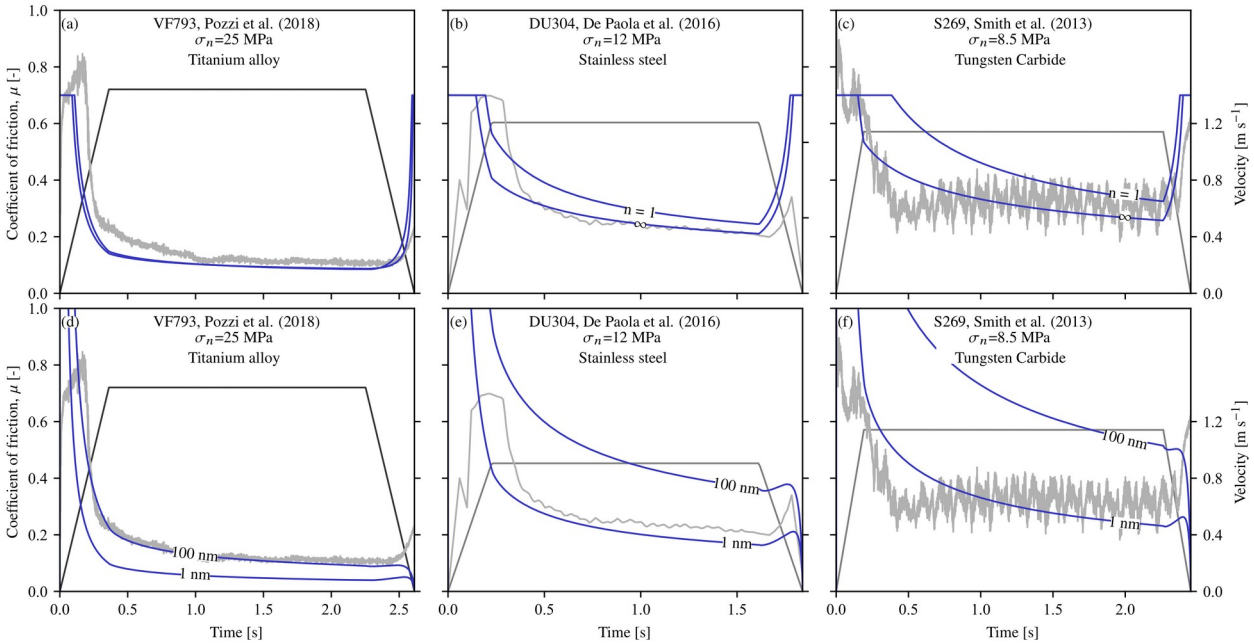


**Figure 7** Effects of varying thermal diffusivity in full thickness models (blue curves) with realistic sample boundary conditions compared to previously published experimental data (grey curves). Panels a) to c) are modelled using the flash heating model described in previous discussion, with fixed thermal diffusivity with curves labelled according to the asperity stress exponent used. Panels d) to f) show the same experimental data, however this time using the

405 GSS model defined in the previous discussion with fixed thermal diffusivity, curves are labelled
406 according to the grain size used in the model prediction. Thermal diffusivity increases from the
407 left to right of the figure.
408
409 For both rheological models we observe that for increasing thermal diffusivity, the fault strength
410 predictions increase, consistently with experimental observations (Figure 7). Generally FH does
411 not predict the initial weakening behaviour, predicting faster weakening in Titanium alloy
412 (Figure 7a) and Stainless steel (Figure 7b), and less abrupt weakening for tungsten carbide
413 (Figure 7c). The differences in model predictions and experimental data may result from strain
414 localisation and grain crushing that occurs during early stages of slip in gouges (Logan et al.,
415 1992). During steady state sliding conditions the FH models are able to predict strength
416 evolution with reasonable success, and in particular predict a slow progressive weakening with
417 slip resulting from a progressive temperature rise, sharing similarities to the experimental data
418 (Figure 7a, b and c). The restrengthening is systematically over predicted by the flash heating
419 models, similarly to the results shown in the previous section.
420
421 Initial weakening is predicted comparatively better for GSS than it is for FH. Similarly to FH, the
422 GSS models also predict progressive weakening observed during constant velocity conditions
423 (e.g. Figure 7e). The restrengthening rate predicted by models is slower than observed in
424 experiments, and consistently with previous discussion of GSS models, strength falls to zero as
425 slip arrests. Generally we observe that the best predictions of fault strength for the gouge
426 experiments are obtained for the previously used parameter set, except at the highest normal
427 stress conditions. Given that we may use the same parameters in the constitutive friction law (FH
428 or GSS), it suggests that the key variable is the bulk temperature evolution. In short, reconciling
429 these individual experimental observations is difficult without carefully considering model

boundary conditions and demonstrates that it is of fundamental importance to accurately capture on and off-fault thermal boundary conditions accurately, confirming the conclusions of Yao et al. (2016).

### 4.4 Transition in weakening mechanisms

Flash heating predictions are better at shorter timescales, whereas longer timescales demonstrate a better prediction by GSS models. In fact all FH models significantly over predict the final strengthening behaviour. Taken together these observations suggest that a transition in weakening mechanisms is likely to occur. At early stages when the bulk fault temperature is low, and GSS is not efficient, behaviour will be dominated by asperity scale flash heating processes leading to bulk heating of the principle slip zone. However as slip and fault temperature increases, GSS deformation becomes increasingly favourable. This transition has been previously proposed by Pozzi et al. (2018) and De Paola et al. (2015), however they did not explicitly consider FH at early stages of slip, suggesting instead that the transition is simply from cataclastic processes to GSS. If FH was active during early stages of slip it is possible that the high contact temperatures during weakening may be sustained during later stages of the experiment and deformation could be accommodated by larger grain sizes. Effectively the two constitutive equations define a threshold temperature at which fault strength approaches a residual strength. In the case of FH this is given by the temperature at which a generic weakening process occurs (which could be GSS), whereas for GSS it defines the temperature at which efficient diffusive mass transfer occurs, in both the governing state variable is fault temperature.

### 4.5 Weakening and restrengthening in basalt

Weakening of basaltic experimental faults is facilitated by frictional melting, which leads to the formation of a hot low viscosity melt layer (Hirose & Shimamoto, 2005; Niemeijer et al., 2011; Rempel & Weaver, 2008; Violay et al., 2019, see videos S3 and S4). Modelling of weakening accommodated by melting has previously addressed by Nielsen et al. (2008) and Rempel & Weaver (2008) who explicitly considered the effects of the effects of progressive melt formation during high velocity sliding. Melting of rock during frictional sliding at high velocity can be shown to result in a complex 2-stage weakening behaviour, reflecting the degree of melt layer formation, with the presence of initially patchy melt leading to strengthening, followed by secondary weakening due to the formation of a continuous meltlayer (Del Gaudio et al., 2009; Hirose & Shimamoto, 2005; Rempel & Weaver, 2008). This is evident in our experiments with slower initial acceleration rates (e.g.$t_s$ = 0.8s, Figure 2f). When acceleration is sufficiently high, then weakening is monotonic (Figure 2d), consistently with Del Gaudio et al. (2009).

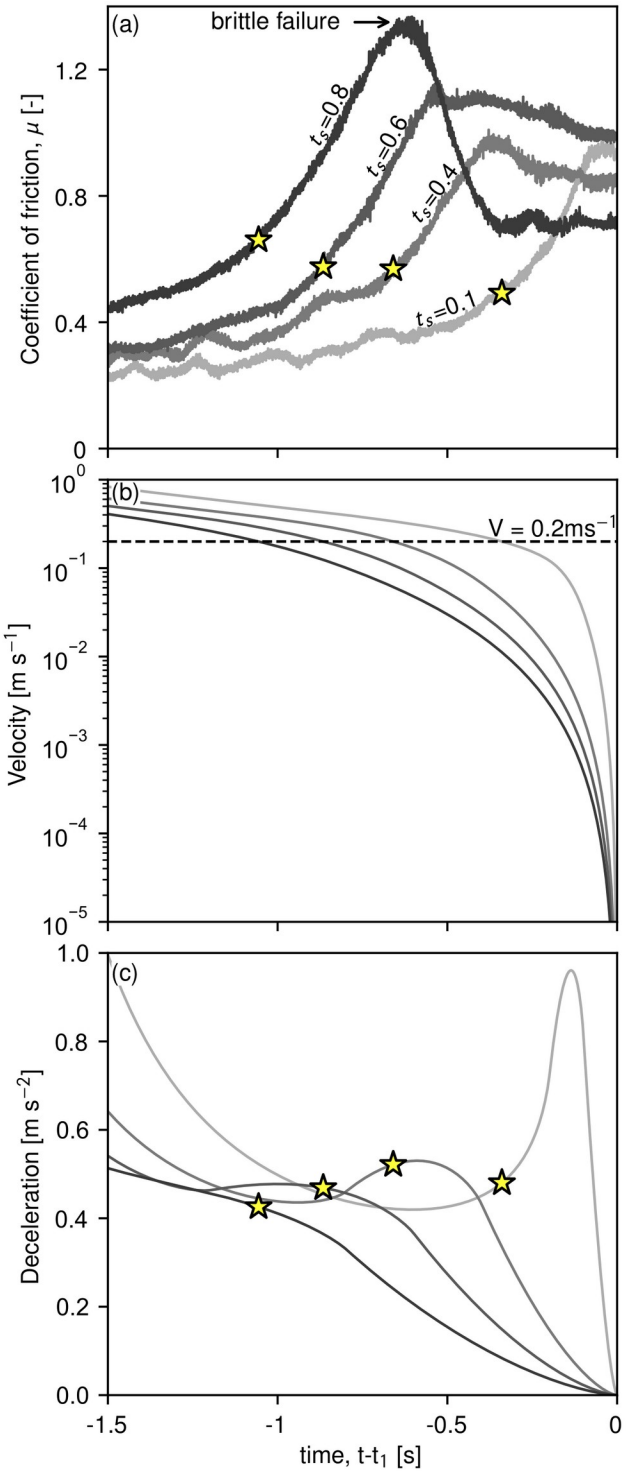


**Figure 8** Restrengthening phase in basalt, illustrating the relationship between final deceleration and restrengthening behaviour in Etna basalt. Curves are coloured according to the smoothing time, stars indicate where slip velocity falls below a critical rate, W (analogous to $V_w$) as defined in Nielsen et al. (2008).

Turning attention now to the restrengthening phase of basalt experiments, we observe a clear relationship between the final deceleration rate and restrengthening behaviour (Figure 8). Where final deceleration is sufficiently rapid, $t_s$ = 0.1 s, then no strength overshoot is observed, and friction monotonically increases up to the end of the experiment, with $\mu_1$ = 0.9. As the deceleration rate is decreased as a result of increasing $t_s$, we observe increasing amounts of strength overshoot, and faster restrengthening rates. For the largest value of smoothing time ($t_s$= 0.8s), the strength overshoot is considerable, with a coefficient of friction close to 1.4 (Figure 8a), almost twice the initial value of $\mu$ = 0.7. Such large increases in strength suggest melt solidification and cohesion of the fault, and where large overshoot was observed cracking was heard, identifying that the melt solidified and failed in a brittle manner (see video S4). In the limit of adiabatic instantaneous deceleration, the fault stress would instantaneously drop as a result of the Arrhenius dependance of melt viscosity (Giordano et al., 2008). However where deceleration is slow, heat diffusion dominates and significant strengthening occurs due to melt solidification. According to Nielsen et al. (2008) frictional melt is expected to form or be sustained above a crictical velocity of approximately 0.2 m $s^{-1}$ for Etna basalt. A velocity of 0.2 m $s^{-1}$ agrees well with the onset of restrengthening in our experiments, with the magnitude correlating well with the timescale faults spend sliding at velocities less than this rate (Figure 8a).

## 5 Are laboratory friction data compatible with elastodynamics?

In the previous section we analysed the potential driving processes that produce the observed evolution of friction in response to an imposed slip history. In nature, during an earthquake, the evolution of frictional strength feeds back into the slip history due to elastodynamic stress

494 redistribution and the requirement of stress equilibrium. To illustrate this, let us consider the
495 elastic stress field associated with anti-plane slip along a fault in 1d:

$$\tau(x,t)=\frac{G}{2c_s}V(x,t)+\int_{\Sigma}\int_{0}^{t}K(x-\xi;t-t')V(\xi,t)dt'dV, \quad (5)$$

496 where $G$ is the shear modulus, $c_s$ is the shear wave speed, $V$ the on fault particle velocity, $x$ is
497 the position along the fault, and $K$ the dynamic load associated to points on the fault that are still
498 slipping.
499
500 The dynamic load term in equation 5 is composed of the integrated slip history across the entire
501 span of the rupturing fault. Waves radiated from other points on the fault results in dynamic
502 loading which modifies slip-stress history, typically resulting in a heterogeneous slip history on
503 the fault plane. In addition, the transfer of stress, wave propagation and rupture velocity depends
504 also on the geometry of the rupturing fault, so that the typical non-planar geometry of natural
505 faults will also influence the slip-stress history (e.g., Romanet et al., 2020). Therefore, slip
506 history at a point on a fault is highly non-unique and depends on the entire integrated rupture
507 history, and in practise there is no unique test of elastodynamic compatibility.
508
509 In order to test the compatibility of our experiments with elastodynamics, we must make several
510 simplifying assumptions. To do this we consider a steady-state slip pulse model, where both the
511 rupture velocity and source duration are constant. In this case the elastodynamic equilibrium in
512 anti-plane geometry can be simplified to

$$\tau(x)=\tau_b+\frac{G}{2\pi V_r}\int_{0}^{L}\frac{V(s)}{s-x}ds, \quad (6)$$

513 where $\tau_b$ is the ambient shear stress, $L$ the pulse length (equivalent to the product of rupture
514 velocity and total rise time), $G^{\iota}$ is the shear modulus multiplied by a function of the ratio of
515 rupture speed $V_r$ and shear wave speed. Equation (6) gives the dynamic elastic stress produced
516 by the slip rate distribution along the pulse. In our experiments, the slip rate is imposed as a
517 function of time. Here we consider that this slip rate evolution represents the relative motion of
518 two opposing points along a steadily propagating pulse. Choosing a constant rupture speed, we
519 first compute the elastic stress by direct integration of (6), and compare it to the measured
520 experimental strength (for details of methodology see Viesca & Garagash (2018) and
521 supplementary material S2). Since strength should be equal to stress during slip to satisfy
522 mechanical equilibrium, any deviations between predicted stress and measured strength would
523 indicate inconsistency between the rheological behaviour of the fault and our choice of imposed
524 slip rate.
525

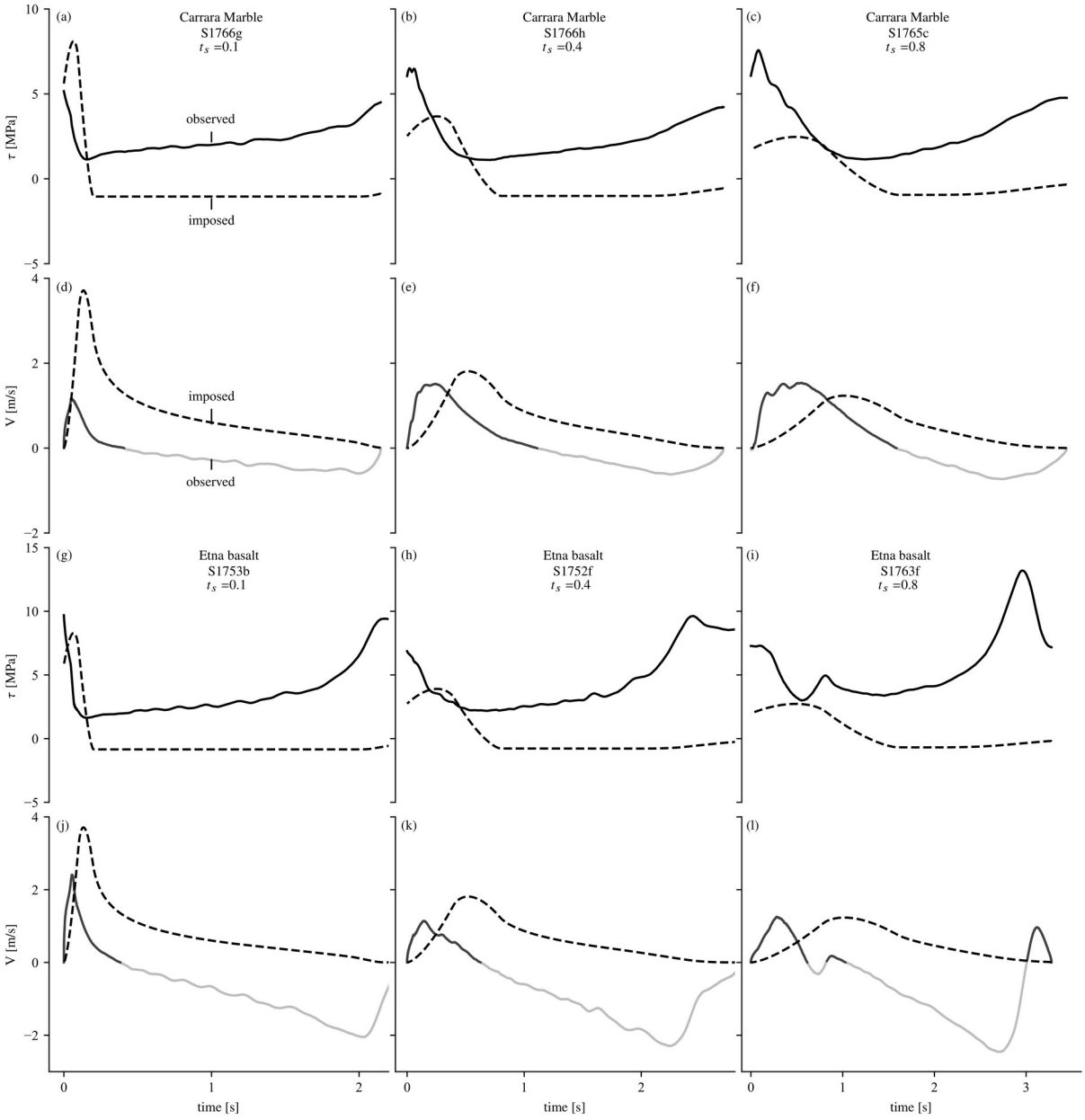


**Figure 9** Experimental data compared to elastodynamic solution using steady state pulse model of rupture propagation. Dashed shear stress curves indicate solutions compatible with the imposed velocity history during an experiment, and overlay smoothed experimental data (solid curves, labelled as observed in a)). The solid velocity history is that which is predicted from the measured evolution of shear stress (traction) during an experiment, lines are coloured grey where $V < 0$ m/s.

The stress predicted by imposing the velocity history is only qualitatively compatible with the overall evolution of strength during tests: there is an initial weakening phase, with strength

decreasing until sliding occurs at constant stress after which the stress increases during final slip deceleration, although the precise magnitudes and timings do not agree. In particular, the predicted final stress increase occurs later than in experimental observations, with a comparatively smaller magnitude.

We can also use our strength measurements to predict what would be the slip rate evolution along a hypothetical pulse, i.e., to determine $V(x)$ based on $\tau(x)$ in (6), assuming this time that strength is equal to elastic stress, and compare this slip rate to the originally imposed experimental slip rate. By imposing zero slip velocity before and after the rupture interval, we also constrain the background stress $\tau_b$ for our hypothetical pulse (see appendix section 3 for details). While there are encouraging similarities between model and observation, the predicted slip rate is quantitatively inconsistent with the imposed one. In particular, the final increase in stress measured in experiments results in back-slip where velocity is negative (e.g. Figure 9k). The prediction of back-slip is not realistic and would not occur during spontaneous rupture.

Overall, the experimental data show limited compatibility with our simple slip pulse model. Considering that the strength is mostly controlled by slip rate (with short state evolution distances) and temperature, we expect that slip rate and strength evolution that are compatible with elastodynamics would involve abrupt changes in slip rate together with rapid strength changes, both at the rupture tip and at the cessation of slip. For instance, in Carrara marble (e.g. Figure 9a and d, sample S1766g), imposing a relatively constant slip rate after initial acceleration will lead to slowly decreasing strength (due to temperature rise), which is likely to eliminate the

558 possibility of back-slip. Then, an abrupt velocity drop might be consistent with an increase in
559 strength above the elastic stress, producing spontaneous slip arrest.
560
561 The results on Etna basalt further support the requirement for rapid final slip deceleration as the
562 strength increases quickly during melt solidification, resulting in a highly unrealistic minimum
563 compatible slip rate of ≈ –2 m/s (Figure 9l), consistent with the notion of melt 'fusion' during
564 high velocity sliding (Fialko & Khazan, 2005).

565 ## 6 Conclusions

566 In this work we document results from high velocity friction experiments imposing a realistic
567 source time history, in order to investigate how fault strength evolves during earthquakes. Simple
568 first order observations show that the weakening distance and breakdown work are inversely
569 dependent on the initial acceleration rate. Experimental results combined with modelling
570 demonstrate that the high velocity strength of faults during variable velocity strongly depends on
571 prior sliding history and temperature evolution. Carbonate built fault strength can be accurately
572 predicted by flash heating at small time scales and grain size sensitive creep at larger timescales,
573 provided that model boundary conditions are faithful to experimental conditions. Where flash
574 heating is utilised to model the fault strength of carbonate built faults, then final restrengthening
575 is always over predicted. In the case that a creep constitutive law is used there are some
576 significant differences between requisite grain sizes for accurate strength predictions and
577 observed grain sizes from microstructural observations (De Paola et al., 2015; Pozzi et al., 2018).
578 This discrepancy remains unresolved, and might be due to incorrect assumptions about our
579 choice of deformation mechanism or the estimated temperature. However, the remarkable

580 agreement between model predictions and observations indicates that thermally activated viscous
581 flow laws are good candidates for the rheology of faults at high velocity.

582 These results provide an important validation of constitutive laws of frictional strength under
583 non-constant velocity histories, justifying their use in coupled elastodynamic models, when the
584 temperature rise of the fault is considered (e.g., Brantut & Viesca, 2017; Noda et al., 2009).

585 In our experiments, we imposed a slip rate history and measured the resulting strength. In nature,
586 there is a feedback between strength and slip rate evolution due to elastodynamic stress
587 redistribution. We tested the consistency of our experimental data with a simple elastodynamic
588 model, and found discrepancies, i.e., the measured strength does not match the predicted elastic
589 stress associated with the imposed slip. It is likely that the rheology of the fault gives rise to
590 velocity changes (acceleration and deceleration) more abrupt than in our imposed source-time
591 functions.

592

## Acknowledgments, Samples, and Data

This project has received funding from the European Research Council (ERC) under the European Union's Horizon 2020 research and innovation programme (grant agreement n° 804685/"RockDEaF" and under the European Community's Seventh Framework Programme (grant agreement n° 614705/"NOFEAR")

All raw experimental data is available at https://zenodo.org/record/4644245

## References

Abercrombie, R. E., & Rice, J. R. (2005). Can observations of earthquake scaling constrain slip weakening? *Geophysical Journal International*, *162*(2), 406–424. https://doi.org/10.1111/j.1365-246X.2005.02579.x

Aretusini, S., Núñez-cascajero, A., Spagnuolo, E., & Tapetado, A. (2020). Fast and localized temperature measurements during simulated earthquakes in carbonate rocks.

Beeler, N. M., Tullis, T. E., & Goldsby, D. L. (2008). Constitutive relationships and physical basis of fault strength due to flash heating. *Journal of Geophysical Research: Solid Earth*, *113*(1), 1–12. https://doi.org/10.1029/2007JB004988

Berman, N., Cohen, G., & Fineberg, J. (2020). Dynamics and properties of the cohesive zone in rapid fracture and friction. *Physical Review Letters*, *125*(12), 125503. https://doi.org/10.1103/PhysRevLett.125.125503

Brantut, N., & Viesca, R. C. (2017). The fracture energy of ruptures driven by flash heating. *Geophysical Research Letters*, *44*(13), 6718–6725. https://doi.org/10.1002/2017GL074110

Candela, T., & Brodsky, E. E. (2016). The minimum scale of grooving on faults. *Geology*, *44*(8), 603–606. https://doi.org/10.1130/G37934.1

Chang, J. C., Lockner, D. A., & Reches, Z. (2012). Rapid acceleration leads to rapid weakening in earthquake-like laboratory experiments. *Science*, *338*(6103), 101–105. https://doi.org/10.1126/science.1221195

Cochard, A., & Madariaga, R. (1994). Dynamic faulting under rate-dependent friction. *Pure and Applied Geophysics PAGEOPH*, *142*(3–4), 419–445. https://doi.org/10.1007/BF00876049

Cverna, F. (2002). *ASM Ready Reference: Thermal Properties of Metals*. ASM International. Retrieved from https://app.knovel.com/hotlink/toc/id:kpASMRRTP1/asm-ready-reference-thermal/asm-ready-reference-thermal

Demurtas, M., Smith, S. A. F., Prior, D. J., Brenker, F. E., & Di Toro, G. (2019). Grain Size Sensitive Creep During Simulated Seismic Slip in Nanogranular Fault Gouges: Constraints

From Transmission Kikuchi Diffraction (TKD). *Journal of Geophysical Research: Solid Earth*, *124*(10), 10197–10209. https://doi.org/10.1029/2019JB018071

Faulkner, D. R., Mitchell, T. M., Behnsen, J., Hirose, T., & Shimamoto, T. (2011). Stuck in the mud? Earthquake nucleation and propagation through accretionary forearcs. *Geophysical Research Letters*, *38*(18). https://doi.org/10.1029/2011GL048552

Fialko, Y., & Khazan, Y. (2005). Fusion by earthquake fault friction: Stick or slip. *Journal of Geophysical Research: Solid Earth*, *110*(12), 1–15. https://doi.org/10.1029/2005JB003869

Fukuyama, E., & Mizoguchi, K. (2010). Constitutive parameters for earthquake rupture dynamics based on high-velocity friction tests with variable sliprate. *International Journal of Fracture*, *163*(1–2), 15–26. https://doi.org/10.1007/s10704-009-9417-5

Del Gaudio, P., Di Toro, G., Han, R., Hirose, T., Nielsen, S., Shimamoto, T., & Cavallo, A. (2009). Frictional melting of peridotite and seismic slip. *Journal of Geophysical Research*, *114*(B6). https://doi.org/10.1029/2008jb005990

Giordano, D., Potuzak, M., Romano, C., Dingwell, D. B., & Nowak, M. (2008). Viscosity and glass transition temperature of hydrous melts in the system CaAl2Si2O8-CaMgSi2O6. *Chemical Geology*, *256*(3–4), 203–215. https://doi.org/10.1016/j.chemgeo.2008.06.027

Goldsby, D. L., & Tullis, T. E. (2011). Flash Heating Leads to Low Frictional Strength of Crustal Rocks at Earthquake Slip Rates. *Science*, *334*(6053), 216–218. https://doi.org/10.1126/science.1207902

Guatteri, M., & Spudich, P. (2000). What can strong-motion data tell us about slip-weakening fault-friction laws? *Bulletin of the Seismological Society of America*, *90*(1), 98–116. https://doi.org/10.1785/0119990053

Han, R., Shimamoto, T., Hirose, T., Ree, J.-H., & Ando, J. -i. (2007). Ultralow Friction of Carbonate Faults Caused by Thermal Decomposition. *Science*, *316*(5826), 878–881. https://doi.org/10.1126/science.1139763

Hirose, T., & Shimamoto, T. (2005). Growth of molten zone as a mechanism of slip weakening of simulated faults in gabbro during frictional melting. *Journal of Geophysical Research: Solid Earth*, *110*(5), 1–18. https://doi.org/10.1029/2004JB003207

Ida, Y. (1972). Cohesive force across the tip of a longitudinal-shear crack and Griffith's specific surface energy. *Journal of Geophysical Research*, *77*(20), 3796–3805. https://doi.org/10.1029/JB077i020p03796

Kanamori, H., & Brodsky, E. E. (2004). The physics of earthquakes. *Reports on Progress in Physics*, *67*(8), 1429–1496. https://doi.org/10.1088/0034-4885/67/8/R03

Kanamori, H., & Rivera, L. (2006). Energy partitioning during an earthquake. *Geophysical Monograph Series*, *170*, 3–13. https://doi.org/10.1029/170GM03

Kostrov, B. V. (1964). Selfsimilar problems of propagation of shear cracks. *PMM*, *28*(5), 889–898.

663 Logan, J. M., Dengo, C. A., Higgs, N. G., & Wang, Z. Z. (1992). *Fabrics of experimental fault*
664 *zones: Their development and relationship to mechanical behavior*. *Fault Mechanics and*
665 *Transport Properties of Rocks* (Vol. 1).

666 Madariaga, R. (2015). *Seismic Source Theory*. *Treatise on Geophysics: Second Edition* (Vol. 4).
667 Elsevier B.V. https://doi.org/10.1016/B978-0-444-53802-4.00070-1

668 Nielsen, S., & Madariaga, R. (2003). On the Self-Healing Fracture Mode. *Bulletin of the*
669 *Seismological Society of America*, *93*(6), 2375–2388. https://doi.org/10.1785/0120020090

670 Nielsen, S., Di Toro, G., Hirose, T., & Shimamoto, T. (2008). Frictional melt and seismic slip.
671 *Journal of Geophysical Research: Solid Earth*, *113*(1), 1–20.
672 https://doi.org/10.1029/2007JB005122

673 Nielsen, S. B., Spagnuolo, E., Smith, S. A. F., Violay, M., Di Toro, G., & Bistacchi, A. (2016).
674 Scaling in natural and laboratory earthquakes. *Geophysical Research Letters*, *43*(4), 1504–
675 1510. https://doi.org/10.1002/2015GL067490

676 Niemeijer, A., Di Toro, G., Nielsen, S., & Di Felice, F. (2011). Frictional melting of gabbro
677 under extreme experimental conditions of normal stress, acceleration, and sliding velocity.
678 *Journal of Geophysical Research: Solid Earth*, *116*(7), 1–18.
679 https://doi.org/10.1029/2010JB008181

680 Noda, H., & Lapusta, N. (2013). Stable creeping fault segments can become destructive as a
681 result of dynamic weakening. *Nature*, *493*(7433), 518–521.
682 https://doi.org/10.1038/nature11703

683 Noda, H., Dunham, E. M., & Rice, J. R. (2009). Earthquake ruptures with thermal weakening
684 and the operation of major faults at low overall stress levels. *Journal of Geophysical*
685 *Research: Solid Earth*, *114*(7), 1–27. https://doi.org/10.1029/2008JB006143

686 Ohnaka, M., Kuwahara, Y., Yamamoto, K., & Hirasawa, T. (1986). Dynamic breakdown
687 processes and the generating mechanism for high frequency radiation during stick-slip
688 instabilities. In *Geophysical Monograph Series* (Vol. 37).

689 Okubo, P. G., & Dieterich, J. H. (1981). Fracture energy of stick-slip events in a large scale
690 biaxial experiment. *Geophysical Research Letters*, *8*(8), 887–890.
691 https://doi.org/10.1029/GL008i008p00887

692 De Paola, N., Holdsworth, R. E., Viti, C., Collettini, C., & Bullock, R. J. (2015). Can grain size
693 sensitive flow lubricate faults during the initial stages of earthquake propagation? *Earth and*
694 *Planetary Science Letters*, *431*, 48–58. https://doi.org/10.1063/1.2756072

695 Passelègue, F. X., Goldsby, D. L., & Fabbri, O. (2014). The influence of ambient fault
696 temperature on flash-heating phenomena. *Geophysical Research Letters*, *41*(3), 828–835.
697 https://doi.org/10.1002/2013GL058374

698 Poirier, J. P. (1985). *Creep of crystals*. *Physics of the Earth and Planetary Interiors* (Vol. 41).
699 https://doi.org/10.1016/0031-9201(85)90106-2

Pozzi, G., De Paola, N., Nielsen, S. B., Holdsworth, R. E., & Bowen, L. (2018). A new interpretation for the nature and significance of mirror-like surfaces in experimental carbonate-hosted seismic faults. *Geology*, *46*(7), 583–586. https://doi.org/10.1130/G40197.1

Proctor, B. P., Mitchell, T. M., Hirth, G., Goldsby, D., Zorzi, F., Platt, J. D., & Di Toro, G. (2014). Dynamic weakening of serpentinite gouges and bare surfaces at seismic slip rates. *Journal of Geophysical Research: Solid Earth*, *119*(11), 8107–8131. https://doi.org/10.1002/2014JB011057

Raj, R., & Ashby, M. F. (1971). On grain boundary sliding and diffusional creep. *Metallurgical Transactions*, *2*(4), 1113–1127. https://doi.org/10.1007/BF02664244

Rempel, A. W., & Weaver, S. L. (2008). A model for flash weakening by asperity melting during high-speed earthquake slip. *Journal of Geophysical Research: Solid Earth*, *113*(11), 1–14. https://doi.org/10.1029/2008JB005649

Rice, J. R. (2006). Heating and weakening of faults during earthquake slip. *Journal of Geophysical Research: Solid Earth*, *111*(5), 1–29. https://doi.org/10.1029/2005JB004006

Rubino, V., Rosakis, A. J., & Lapusta, N. (2017). Understanding dynamic friction through spontaneously evolving laboratory earthquakes. *Nature Communications*, *8*(May), 1–12. https://doi.org/10.1038/ncomms15991

Schmid, S. M., Boland, J. N., & Paterson, M. S. (1977). Superplastic flow in finegrained limestone. *Tectonophysics*, *43*(3–4), 257–291. https://doi.org/10.1016/0040-1951(77)90120-2

Scholz, C. H. (2002). *The Mechanics of Earthquakes and Faulting*. *The Mechanics of Earthquakes and Faulting*. https://doi.org/10.1017/cbo9780511818516

Smith, S. A. F., Di Toro, G., Kim, S., Ree, J. H., Nielsen, S., Billi, A., & Spiess, R. (2013). Coseismic recrystallization during shallow earthquake slip. *Geology*, *41*(1), 63–66. https://doi.org/10.1130/G33588.1

Sone, H., & Shimamoto, T. (2009). Frictional resistance of faults during accelerating and decelerating earthquake slip. *Nature Geoscience*, *2*(10), 705–708. https://doi.org/10.1038/ngeo637

Spagnuolo, E., Plümper, O., Violay, M., Cavallo, A., & Di Toro, G. (2015). Fast-moving dislocations trigger flash weakening in carbonate-bearing faults during earthquakes. *Scientific Reports*, *5*, 1–11. https://doi.org/10.1038/srep16112

Tinti, E., Fukuyama, E., Piatanesi, A., & Cocco, M. (2005). A kinematic source-time function compatible with earthquake dynamics. *Bulletin of the Seismological Society of America*, *95*(4), 1211–1223. https://doi.org/10.1785/0120040177

Tinti, E., Spudich, P., & Cocco, M. (2005). Earthquake fracture energy inferred from kinematic rupture models on extended faults. *Journal of Geophysical Research*, *110*(B12), B12303. https://doi.org/10.1029/2005JB003644

738 Di Toro, G., Han, R., Hirose, T., De Paola, N., Nielsen, S., Mizoguchi, K., et al. (2011). Fault
739 lubrication during earthquakes. *Nature*, *471*(7339), 494–499.
740 https://doi.org/10.1038/nature09838

741 Di Toro, Giulio, Goldsby, D. L., & Tullis, T. E. (2004). Friction falls towards zero in quartz rock
742 as slip velocity approaches seismic rates. *Nature*, *427*(6973), 436–439.
743 https://doi.org/10.1038/nature02249

744 Tsutsumi, A., & Shimamoto, T. (1997). High-velocity frictional properties of gabbro.
745 *Geophysical Research Letters*, *24*(6), 699–702. https://doi.org/10.1029/97GL00503

746 Viesca, R. C., & Garagash, D. I. (2018). Numerical Methods for Coupled fracture problems.
747 *Journal of the Mechanics and Physics of Solids*, *113*, 13–34.
748 https://doi.org/10.1016/j.jmps.2018.01.008

749 Violay, M., Nielsen, S., Spagnuolo, E., Cinti, D., Di Toro, G., & Di Stefano, G. (2013). Pore
750 fluid in experimental calcite-bearing faults: Abrupt weakening and geochemical signature of
751 co-seismic processes. *Earth and Planetary Science Letters*, *361*, 74–84.
752 https://doi.org/10.1016/j.epsl.2012.11.021

753 Violay, M., Passelègue, F. X., Spagnuolo, E., Di Toro, G., & Cornelio, C. (2019). Effect of water
754 and rock composition on re-strengthening of cohesive faults during the deceleration phase
755 of seismic slip pulses. *Earth and Planetary Science Letters*.

756 Yao, L., Ma, S., Platt, J. D., Niemeijer, A. R., & Shimamoto, T. (2016). The crucial role of
757 temperature in high-velocity weakening of faults: Experiments on gouge using host blocks
758 with different thermal conductivities. *Geology*, *44*(1), 63–66.
759 https://doi.org/10.1130/G37310.1

760 Yoffe, E. H. (1951). LXXV. The moving griffith crack. *Philosophical Magazine Series 7*,
761 *42*(330), 739–750. https://doi.org/10.1080/14786445108561302

762